

Study of Microstructural Evolution and Strain Analysis in SiO_x/C Negative Electrodes Using In-situ X-ray Tomography and Digital Volume Correlation

Abhilash Valisammagari,^{*[a, b]} Joel Lachambre,^[a] Jerome Adrien,^[a] Ludovic Broche,^[c] Martin Petit,^[b] Vivien Esnault,^[b] and Eric Maire^[a]

Increasing the silicon content in batteries is expected to enhance their capacity. However, its implementation comes with challenges, as silicon exhibits a large volumetric expansion. This expansion is a significant factor contributing to the decreased lifespan of these batteries. One of the critical degradation mechanisms from a mechanical perspective is the delamination of electrode structure. The cyclability of these negative electrodes is noted to be influenced by the interaction between the binder and particles during battery cycling. The heavy local strain experienced by particles in these electrodes often leads to binder failure, resulting in particle isolation, detachment, or delamination over multiple cycles. A good

understanding of the local evolution of the strain is essential in advancing the mechanical modelling of the degradation mechanism and in realizing the complete potential of silicon-based electrodes. In this work, in situ global and local strain measurements were performed by combining synchrotron tomography with Digital Volume Correlation (DVC). The measurements showed that there is significant local strain in these electrodes which can lead to delamination. In addition to this, the spatial variability of the composite electrodes was characterized by estimating the characteristic length to strain, which can be used to replicate the strain field and model the delamination.

1. Introduction

In the transition towards the decarbonization of energy and transportation sectors, there is an increasing demand for high-capacity storage systems. Lithium-ion batteries are currently playing a pivotal role in accelerating this transition. Several avenues are being explored to improve the capacity, battery life, and safety, while simultaneously reducing the cost of these storage systems. Several technologies are anticipated in the battery market, and the different steps leading to major improvements are categorized into the so called "battery generations".^[1] In this framework, a notable amount of research and development is focused on improving the capacity of the negative electrode materials for future generations of Li-ion batteries. One of the promising approaches is the incorporation

of silicon in the negative electrodes. Specifically, within the framework of battery generations, generation 3b (Gen3b) aims to enhance the performance of liquid batteries by improving the active materials used (both at positive and negative), particularly in the case of the negative electrodes, the performance enhancement is achieved by including high amounts of silicon beyond 20%.^[1]

Graphite is traditionally the most commonly used negative electrode material in Li-ion batteries owing to its excellent conductive properties. It hosts lithium ions in the gaps between its layered structure by a process called intercalation, reaching a specific capacity of ~372 mAh g⁻¹ for LiC₆.^[2,3] Whereas, alloying materials such as silicon hosts lithium by forming several alloying compounds with it. At room temperature, the theoretical maximum specific capacity when silicon is completely lithiated to form Li_{3.75}Si is ~3579 mAh g⁻¹.^[4,5] This capacity is nearly 10 times higher than that of graphite. However, employing silicon particles directly is not preferred due to its volumetric expansion during lithiation (~300%). This expansion leads to the initiation of several degradation mechanisms in the electrodes, such as particle cracking, delamination, and irreversible consumption of lithium (for the formation of Solid Electrolyte Interface (SEI)), gradually reducing the power and capacity of these batteries.^[6,7] Many innovative mitigation strategies (such as nano-structuring, surface modification, proper electrolyte and binder selection etc.) were researched to implement silicon as the negative electrode material.^[8] Though the performance of the electrode was good with nanoparticles, these solutions are not economical for mass production. One of the commercially accepted solutions is to use a composite material with SiO_x (> 20 wt%) and graphite. The composite

[a] A. Valisammagari, J. Lachambre, J. Adrien, E. Maire
INSA-Lyon, MATEIS UMR CNRS 5510, 20 Avenue Albert Einstein, 69621, Villeurbanne, France
E-mail: abhilash.valisammagari@insa-lyon.fr

[b] A. Valisammagari, M. Petit, V. Esnault
Department of physical chemistry and mechanics, IFP Energies Nouvelles, Rond-point de l'échangeur de solaize, 69360, Solaize, France

[c] L. Broche
The European Synchrotron Radiation Facility (ESRF), 71 Av. des Martyrs, 38000, Grenoble, France

Supporting information for this article is available on the WWW under <https://doi.org/10.1002/batt.202400416>

© 2024 The Authors. Batteries & Supercaps published by Wiley-VCH GmbH. This is an open access article under the terms of the Creative Commons Attribution Non-Commercial License, which permits use, distribution and reproduction in any medium, provided the original work is properly cited and is not used for commercial purposes.

nature of these electrodes offers a combination of good capacity and stability. It was observed that during the initial reaction of SiO_x with lithium, the reaction products (Li₂O and some lithium silicates) in this system are observed to buffer the effects of silicon volume expansion.^[9] While a high amount of graphite improves conductivity.

Concerning the substantial variation in the volumetric expansions of approximately 100–180% for silicon oxide^[10,11] and 10% for graphite,^[12] the heterogeneity in the local deformations can lead to delamination and other binder-related failure mechanisms. Insights into the evolution of the local and global strain at the electrode scale are crucial when trying to model the mechanical degradation in the active material. To assess global strain evolution in electrodes, researchers have employed electrochemical dilatometry, which provides high-precision data on electrode thickness variations.^[13] However, this technique falls short in providing insights into the localized displacements within the active material of the electrode. Apart from this, X-ray Computed Tomography (XRCT) is a powerful, non-destructive technique essential for characterizing the local variations in composite electrodes. When aiming for extremely high spatial and temporal resolutions, synchrotron source X-rays offer a practical method. These are highly brilliant and coherent X-rays that enable high speed image acquisition with good contrast. In situ and operando studies were performed using synchrotron sources enabling the observation of microstructural changes in the electrode.^[14] The lithiation and delithiation dynamics were studied at the particle scale revealing the expansion behavior and crack formation in the particles.^[15,16] Characterization techniques combining X-Ray Diffraction (XRD) and tomography were used to identify the phase distributions within electrodes, mainly tracking the evolution of silicon phases.^[17]

For non-destructive inspection of displacement fields, optical techniques like Digital Image Correlation (DIC) have proven effective. This technique relies on the identification and tracking of features between undeformed and deformed images, allowing for precise measurement of localized displacement and strain in materials. In image correlation techniques, the choice of imaging technique enables a broad range of measurement sensitivity and resolution.^[18] An extension of this method, 3D Digital Volume Correlation (DVC), integrates DIC with 3D volume images from X-ray tomography. In battery research, image correlation techniques have recently been applied to measure strain in electrodes at various scales. At the particle scale, in situ evolution of strain was mapped in the nanoparticles using Coherent X-ray Diffraction Imaging (CXDI).^[19,20] 2D strain fields on a graphite electrode surface were estimated by combining optical microscopy and DIC.^[21] At cell level, 3d-DIC was performed using multiple synchronized stereo sensors to gain a complete description of volume change in the li-ion polymer pouch cells.^[22] By combining DVC and X-ray tomography, strain evolution in the batteries was observed at electrode scale.^[23–26] Paz-Gracia et al.^[24] performed X-ray tomography on the silicon containing electrode and identified various morphological features such as changes in the gray scale of the silicon particles during lithiation. Later they used DVC to

identify the evolution of volumetric strain in the electrodes. Similar investigation was performed by Pietsch et al.^[26] identifying the local displacements and volumetric strain in the silicon graphite composite electrode using DVC. Eastwood et al.^[25] performed DVC over the timelapse images from laboratory tomographs of a manganese oxide cathode at electrode scale and mapped its displacement field.

In the current study, the microstructural properties of the SiO_x/C electrode were characterized by utilizing a laboratory tomography. Following this, we conducted *in situ* X-ray tomographic analysis at the European Synchrotron Radiation Facility (ESRF) ID19 beamline to evaluate the evolution of global strain in the electrode. Finally, by employing DVC, we investigated (at the electrode scale) the spatial distribution of the local strain fields and dynamic evolution of the composite electrode during its cycling.

Experimental Section/Methods

Electrode Preparation

For the preparation of active material mixture, commercially available SiO_x–C composite powder was used.^[11,27] According to the supplier datasheet,^[27] this powder was composed of 5–20 wt% of silicon monoxide particles and 80–95 wt% of graphite flakes (material density 2.08–2.30 g/cm³ at 25 °C). To enhance the electrode's electrical conductivity, carbon black sized between 0.5–0.9 μm was added into the active material mixture. The aqueous negative electrode slurry was prepared by adding 94 wt% of the active material with 2 wt% carbon additive, and 1.5 wt% carboxymethyl cellulose (CMC) (derived from a 5% CMC solution in water). Approximately 40 wt% of water was gradually added to this mixture and properly mixed in the thinky planetary mixer at 2000 RPM followed by degassing at 800 RPM. Later, 2.5 wt% styrene-butadiene rubber (SBR) was added to this slurry and re-passed to the mixer with the same protocol as mentioned previously. Water was gradually added until the desired slurry viscosity was achieved. The prepared slurry was coated over a copper foil to a thickness of 100 μm. This coating was dried in two steps: initially at 55 °C for 1 h and then, to eliminate any residual water trapped in the electrode, the second drying step was conducted at 85 °C under vacuum for 24 h. The final dried electrode consisted of areal mass loading of 8.5 g cm⁻². The electrodes prepared in this study are not calendared. Although the literature suggests that calendaring improves electrochemical performance by consolidating the dried coating,^[28] it may introduce variability in the measurement of local strain.

Preparation of Swagelok Cell

Figure 1 shows a schematic of a swagelok cell, with the body of the swagelok made up of PFA, which does not attenuate much of the X-rays, making them the ideal cells for conducting *in situ* experiments on batteries. They were widely employed by numerous researchers for this purpose.^[29,30] The dried electrode, glass fiber, and lithium metal were cut into discs of 3 mm diameter and passed for assembly in the argon-filled glove box. Initially, the separator was soaked in electrolyte (1 M lithium hexafluorophosphate (LiPF₆) dissolved in ethylene carbonate (EC): ethyl methyl carbonate (EMC) (3:7) (vol.), with additives 10 wt% fluoro ethylene carbonate (FEC) and 2 wt% vinylene carbonate (VC)). Inside the central body of the swagelok cell, the half-cell was stacked by positioning the electro-

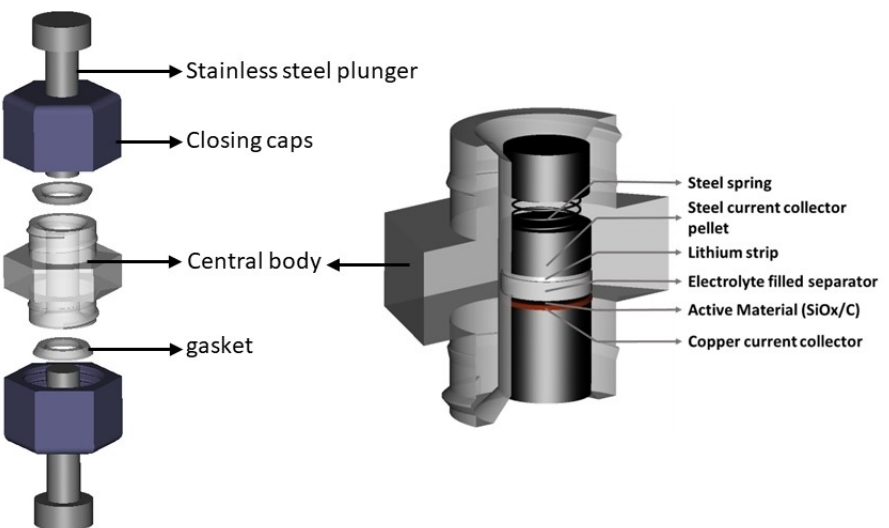


Figure 1. Schematic of the swagelok cell assembly showing electrode stack in the central body.

lyte-filled separator between the prepared electrode and the lithium metal strip. Pressure was applied to the stack with the help of a spring, and the assembly was sealed tightly using closing caps and a gasket. A steel pellet was employed between the spring and the lithium strip to maintain a uniform distribution of pressure. The amount of pressure applied to the stack is hard to regulate reliably. To establish connections with the external circuit, a stainless-steel plunger was provided on both ends. A similar protocol was used for stacking the coin cells used in this study.

Protocol for Electrochemical Performance Testing

Formation step

For the complete formation of SEI and other lithiation products, initially A formation step was performed over the prepared cells at a slow charging rate of C/10, at a temperature of 65°C. For this step, initially constant voltage of 2 V is applied over the cell for 4 h continuing with a constant current lithiation of active material at C/10 until the cell potential reaches 0.01 V. subsequently, a constant voltage of 0.01 V is applied for 2 h continuing with constant current delithiation at C/10 until the cell reaches a potential of 1 V.

Cycling

The cycling is performed between 0.01 V and 1 V at ambient temperature. The electrochemical cycling window is selected based on the literature.^[11,30] Within the specified cycling window, a constant current constant voltage (CCCV) protocol was employed during lithiation (discharge), and a constant current (CC) protocol was used for delithiation (charge) of the prepared half-cells. A charge/discharge rate of C/6 and C/3 was chosen for the coin cells. Whereas for the swagelok cells it was C/3, this is chosen to save the time at the synchrotron.

Experiment Settings for Laboratory Tomography

Laboratory experiments were performed using an EasyTom Nano tomograph (Rx Solutions, France) (with a pixel size of 0.3 μm) over the non-cycled and cycled electrode samples at several states of charge. Small samples were carefully cut from the electrode using a

doctor blade and were glued onto the top of a thin and long rod (of diameter 1 mm, length 10 cm) sample support. The sample along with its support was assembled on the sample holder between an X-ray source (Hamamatsu tube equipped with a LaB₆ emission tip) and a charge coupled device (CCD) detector. The tube voltage and current were set to 50 kV and ~150 μA respectively to achieve a target current of ~20 μA. The exposure time of the CCD detector was set to ~1 s and the image acquisition was performed continuously without pausing the sample rotation. By adjusting the distance between the sample-detector and the sample to source a pixel size of 0.3 μm was achieved. A total of 3008 2D projections were taken over a 360° sample rotation leading to a total scan time of approximately 1 h per sample. The reconstruction was performed using Xact software (from RX Solutions).

Experimental Settings for ESRF ID19 Beamline

The *in situ* XRCT experiments were performed at the ESRF ID19 beamline. The swagelok cells were mounted over the goniometer on the sample stage between the source and the detector. The sample's region of interest, i.e., the active material region was aligned using a goniometer. This alignment was crucial to prevent any interference from the metal current collectors during the experiments. For the tomographic acquisition, the synchrotron beam was set to 26.5 keV and is projected over the central region of the swagelok cell. Over 180° of sample rotation, 1000 2D projections were captured, with 90 milliseconds of exposure time per projection. Which represents the total scan time of 90 s/scan. The exposure time and the beam energy were set to the presented values to avoid beam damage to the material which is also seen in the literature.^[31] A PCO Edge 5.5 CMOS camera equipped with 20 μm GGG scintillator was used at the detector to capture the projections. with a 10x magnification, a pixel size of 0.65 μm was achieved. The size of the acquired tomographic volume was 1170×1170×1079 μm³. The tomographic reconstruction was performed with an in-house developed reconstruction software nabu/tomwer of ESRF. Prior to the reconstruction, the center of rotation of the samples were optimized by overlaying and comparing the 0° and 180° images. The resulting data was stored in 16-bit tiff image format and was post-processed using Fiji software.

DVC and Strain Estimation

DVC is an optical technique used to estimate the displacement fields by comparing the deformed image to the undeformed (reference) image. Considering two images F (reference image) and G (deformed image) deformed due to the displacement field of U_{exp} . The displacement field is obtained by solving the optical flow equation shown below which assumes that the change in grey level in a region is due to the displacement of the pixels. Equation (1)

$$f(x) = g(x + u(x)) \quad (1)$$

This problem is solved using the least square method by minimizing the residue φ_c^2 .^[32] Equation (2)

$$\Phi_c^2(u) = \frac{1}{2} \int_{\Omega} [f(x) - g(x + u(x))]^2 d\Omega \quad (2)$$

Further details on solving the equation are provided in the reference.^[32] A similar procedure is repeated for multiple scales to avoid local minimum and to overcome the limitation of linearization. Once a convergence is reached over the incremental displacement du , the correlation provides a displacement field and residue which gives us an idea of the quality of the correlation. The residue helps to detect sudden variations in the brightness or contrast between the images or the appearance of cracks or damage in the sample. Here pyedic python module,^[33] developed by Joel Lachambre of INSA Lyon was used for performing DVC on the tomography data. The DVC performed uses a global approach^[34] based on a description of displacement field using a C8 element mesh and its shape functions. The mesh size selected is a trade-off between measurement uncertainty and the required spatial resolution. In the current study, a constant element size of 5.2 μm was used for all the samples. The calculations were performed between each timestep and initial reference timestep from the in-situ tests. Regularization is performed over a larger number of pixels to minimize the uncertainty in the estimation of displacements.

The 3d displacement tensor ' u ' is measured using DVC in different locations inside the sample. The information of the local strain can then be determined everywhere in the analyzed volume. The local strain tensor (ϵ) can be calculated as the gradient of the displacement tensor (refer Equation (3) below).

$$\epsilon = \frac{1}{2} ((\nabla u)^T + \nabla u) = \begin{bmatrix} \epsilon_{xx} & \epsilon_{xy} & \epsilon_{xz} \\ \epsilon_{yx} & \epsilon_{yy} & \epsilon_{yz} \\ \epsilon_{zx} & \epsilon_{zy} & \epsilon_{zz} \end{bmatrix} \quad (3)$$

Where, the diagonal components ϵ_{xx} , ϵ_{yy} , and ϵ_{zz} represent the normal strain along the x, y, and z directions respectively. The non-diagonal components ϵ_{xy} , ϵ_{yz} , and ϵ_{xz} represent shear components in the xy, yz, and xz planes respectively. From the obtained strain tensor two invariants were computed. Firstly, the volumetric strain (ϵ_v) which is computed from the trace of strain tensor as shown in the Equation (4) and represents the local changes in volume. Secondly, the von mises equivalent strain (ϵ_{eq}) which represents total localized strain intensity and is computed as shown in Equation (5).

$$\epsilon_v = \frac{\nabla V}{V} = \text{tr}(\epsilon) = \epsilon_{xx} + \epsilon_{yy} + \epsilon_{zz} \quad (4)$$

$$\begin{aligned} \epsilon_{dev} &= \epsilon - \frac{1}{3} \text{tr}(\epsilon) I \\ \epsilon_{eq} &= \sqrt{\frac{2}{3} \epsilon_{dev} : \epsilon_{dev}} \end{aligned} \quad (5)$$

Where, ϵ_{dev} is the deviatoric component of strain tensor.

2. Results and Discussion

2.1. Electrode Performance

The electrode's performance was assessed using coin cells, as outlined in the **experimental section**. Since all the electrodes presented in this study are half cells with lithium as the counter electrode, for simplicity, instead of charge/discharge, delithiation/lithiation of active material is used respectively. Figure 2A, and B shows the evolution of lithiation/delithiation profiles and capacity evolution of the SiOx/C material with cycling. During the formation step at C/10 (represented as cycle number zero), on lithiation, a huge initial capacity of $800 \pm 50 \text{ mAh g}^{-1}$ was observed. At the end of the formation step on delithiation, the electrode lost a lot of its capacity due to the consumption of the electrolyte for the formation of SEI and initial irreversible reaction products, reaching a final value of $650 \pm 20 \text{ mAh g}^{-1}$. The coulombic efficiency (CE) (ratio of capacity during de-lithiation to the capacity during lithiation), during the formation step was observed to be above 75% which is in line with the material expectation from manufacturer datasheet. After the formation of the cells, cycling was conducted at both C/3 and C/6. As shown in Figure 2B a comparison of capacity evolution was made during the initial nine cycles for both the C-rates (refer to the supporting data Figures S1, S2 for the electrode capacity evolution during the first 50 cycles). During the first cycle, the capacities of the electrodes were lower (C/6: $440 \pm 20 \text{ mAh g}^{-1}$, and C/3: $320 \pm 20 \text{ mAh g}^{-1}$), with a CE of around 90% and above. The capacities quickly increased during the initial 5 cycles (by stabilizing at $\approx 500 \text{ mAh g}^{-1}$ for C/6 and $\approx 400 \text{ mAh g}^{-1}$ for C/3) showing that silicon is active while reaching a CE above 99%. Later, in the next cycles starting from cycle 5, the capacity started to decrease gradually. In general, the capacities achieved during cycling at C/6 were higher compared to that at C/3 which is expected due to the kinetic limitations.

2.2. Microstructural Characterization

To comprehensively investigate the microstructure of the electrode material, a post-mortem tomographic analysis was conducted with a pixel size of 0.3 μm. Figure 3A shows the electrode sample before any electrochemical cycling. The different active material regions segmented using Fiji Weka segmentation are highlighted in the Figure 3A. II. The difference in contrast between silicon oxide and graphite regions is attributed to their differences in X-ray attenuation/absorption.

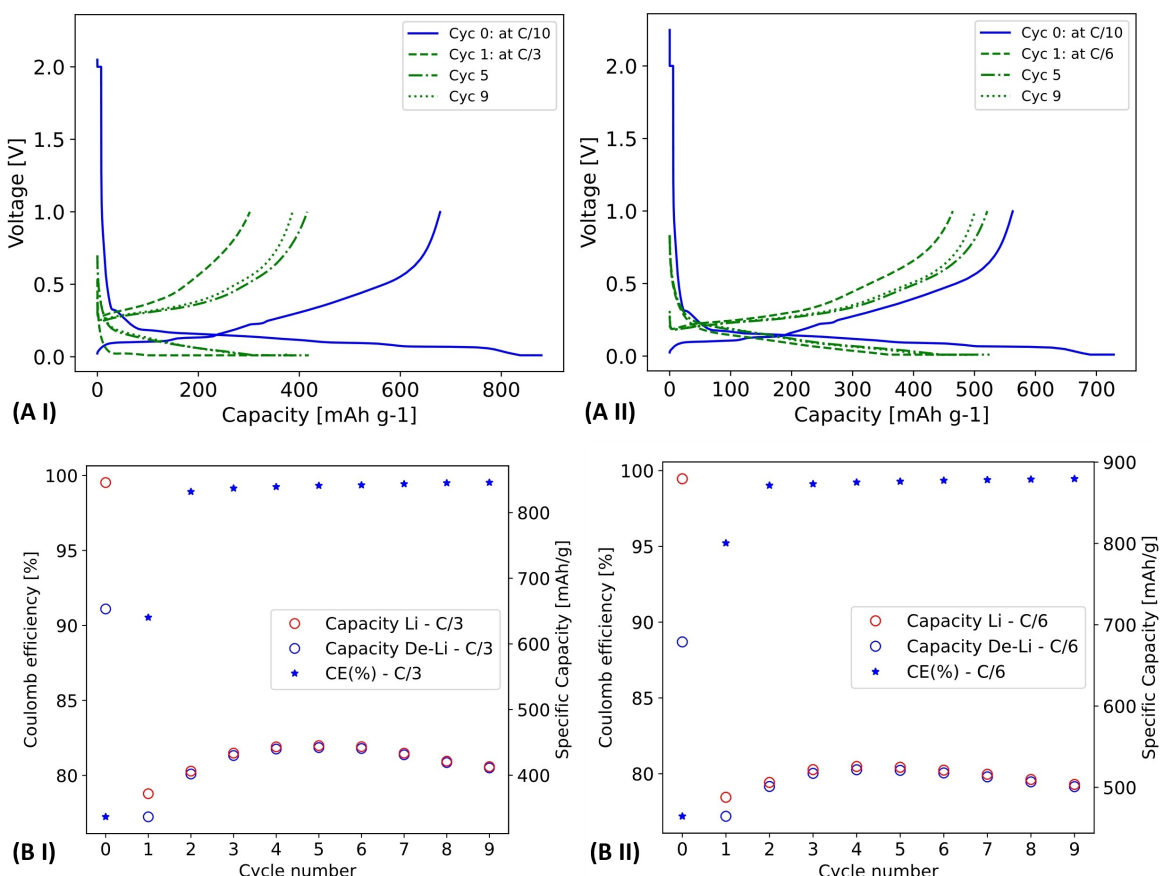


Figure 2. (A) Evolution of lithiation/delithiation profiles of SiO_x/C and graphite composite electrode at C/3 (I) and C/6 (II) during 1st, 5th, and 9th cycles. (B) Evolution of lithiation/delithiation capacities and coulombic efficiency with cycles for C/3 (I) and C/6(II).

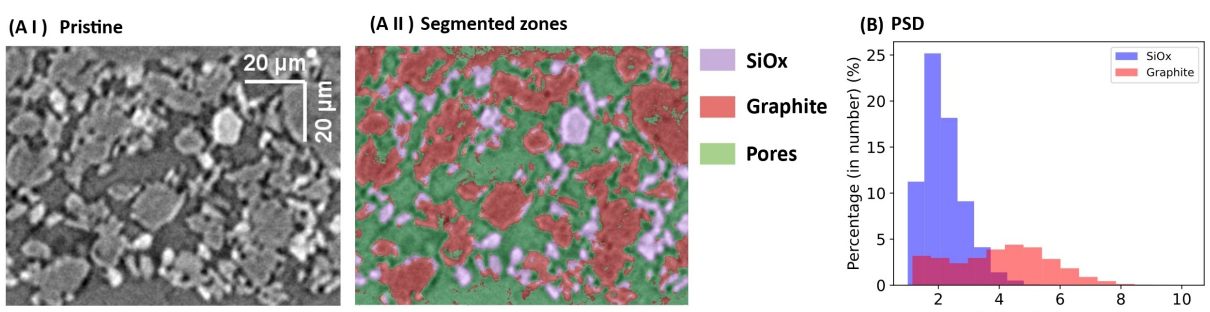


Figure 3. (A. I) Pristine electrode sample slice (scale bar: 20 μm) (A. II) segmented regions of the pristine electrode showing graphite (colored in red), SiO_x (colored in purple) and pore space (colored in green); (B) Particle size distribution derived from the pristine sample representing the number percentage of each particle size within the total cumulative count of all particles.

A comparison of the mass attenuation coefficients of all the materials in the electrode are presented in the supporting data Table S1. The grayscale in the images was selected in such a way that the regions of higher attenuation (such as SiO_x) appear bright, and regions of lower attenuation (pore space) appear darker. Graphite appears with an intermediate gray level. Note that binder, also present in these electrodes, cannot be distinguished from graphite as it appears with a similar gray level. In addition, the percentage of binder is very low (4%) and is impossible to identify at this resolution. A small sub-volume

of 100×100×85 μm^3 was extracted from the electrode images to perform granulometry. Within the sample volume, the volume fractions of SiO_x, graphite, and porous region were estimated, and they correspond to 11.07% for SiO_x, 52.94% for graphite, and the remaining volume being porous space. The particle sizes were evaluated from the representative sphere volumes and are presented in the Figure 3b. The mean particle sizes of SiO_x and graphite were measured to be 1.5 μm and 4 μm respectively. The true sphericity (Ψ) of the particles was calculated as = S_n/S . Where, S_n is the nominal surface area (

$\sqrt[3]{36\pi}V.2)$ representing the surface area of the sphere having the same volume as the object and, S is the actual surface area of the object.^[35] The average sphericity was measured to be 0.8 and 0.45 respectively for SiO_x and graphite particles.

To study the evolution of active material lithiation through tomography, electrode samples were collected at various States of Lithiation (SOL) during the 1st, 10th, and 21st cycles. SOL estimation was based on capacities recorded from prior cycles and the voltage-capacity profiles of the electrode. Lithiation was stopped in each coin cell upon reaching the target capacity, and the electrode samples were subsequently washed in dimethyl carbonate (DMC) for 2 min within the glove box before being transferred for tomography. Imaging was conducted using the similar beam settings as employed for the pristine electrode and are presented in Figure 4. (the details on capacities and SOL estimation of each sample are provided in the Section 2 of supporting data).

Figure 4A shows the tomographic slices taken at different states of lithiation [SOL 25–100%] during the first cycle. In comparison to the pristine electrodes during increased lithia-

tion, a shell with relatively low contrast surrounding the bright SiO_x core was observed (see zoomed-in regions numbered 'i' for each slice in Figure 4). This core-shell structure was less prominent or absent in SiO_x particles with SOL below 50%. To verify this observation, additional images captured from cells during the 10th cycle at various SOLs are presented in Figure 4B. The images revealed a consistent formation of less attenuating core-shell structures with increased lithiation of SiO_x particles, this could be likely attributable to variations in attenuation coefficients during lithiation (refer to supporting data Table S1 on attenuation coefficients of lithiated products). Such attenuation changes and core-shell formations have already been reported in the literature for silicon-containing electrodes.^[36,37] Figure 4C illustrates the fully lithiated state (SOL $\approx 100\%$) at the 21st cycle, qualitatively revealing a significant reduction in the contrast of SiO_x particles, making them less distinguishable compared to pristine samples. A small region with particles of varying contrasts is highlighted in Figure 4C I.i, where graphite is marked in red, bright SiO_x in blue, and three other SiO_x particles in yellow which exhibit different grey levels.

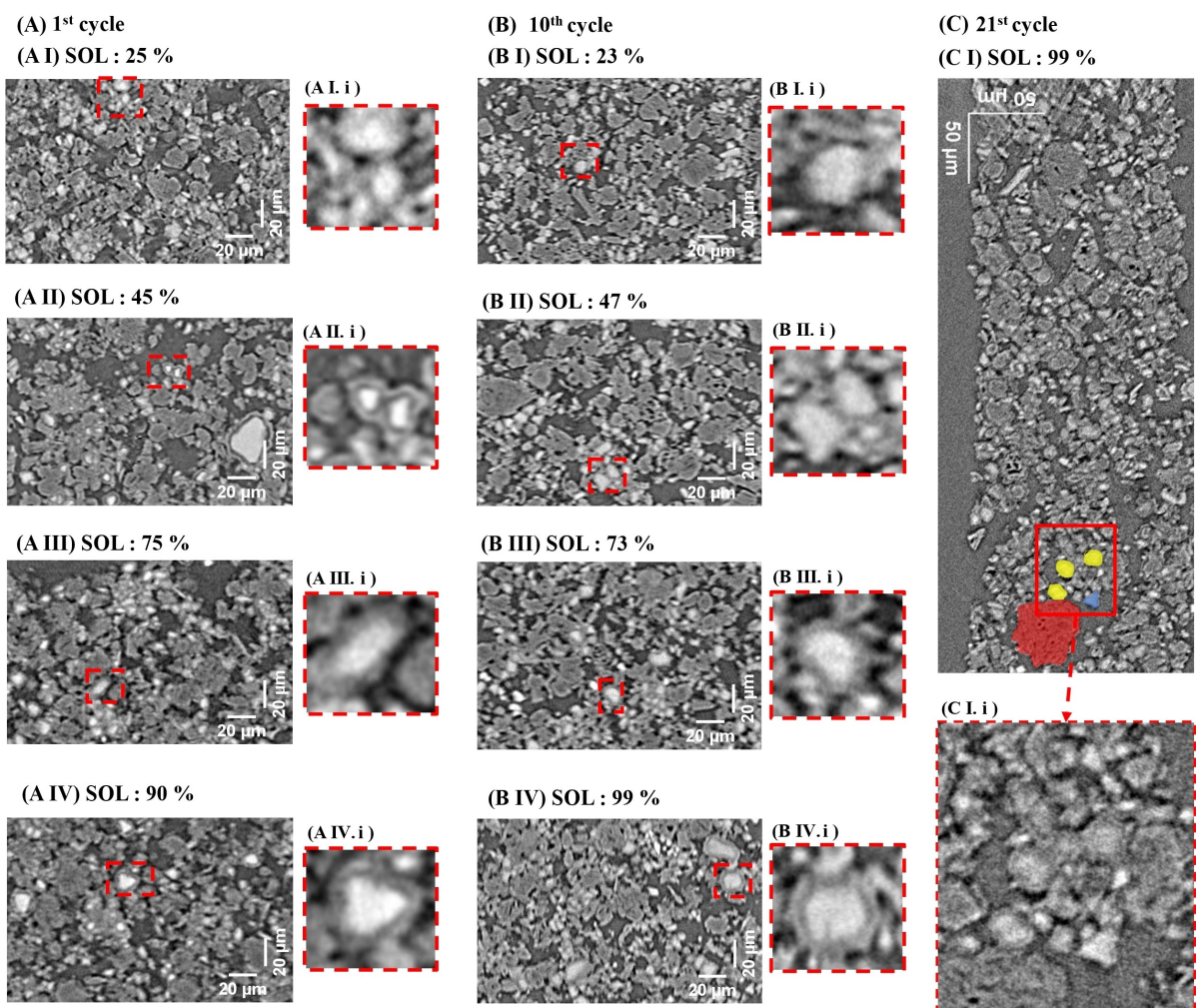


Figure 4. Tomographic slices taken from samples at different states of lithiation during the (A, B) 1st and 10th cycle with zoomed-in regions of the samples showing (i, red box) variation in attenuation of SiO_x particles (scale bar: 20 μm). (C) Tomographic slice from the sample at the 21st cycle completely lithiated state showing contrast differences between (red) graphite, (blue) bright SiO_x , and (yellow) low-attenuating SiO_x and (C i.i) the zoomed-in section of the highlighted zones.

These grey level differences are presumed to be due to the different levels of lithiation. Although precise identification of the chemical species in the lithiated electrodes requires further chemical analysis which is not doable using polychromatic X-ray tomography and is beyond the scope of current study.

From the completely lithiated states of the 1st, 10th and 21st cycles presented in Figure 4(A IV, B IV and C), certain SiO_x particles exhibited no change in attenuation, which could be due to the reduced participation in lithiation and potentially indicate electrical isolation. Furthermore, certain SiO_x particles as prominently seen in Figure 4(A II. i) display a discontinuity between their outer shell and core, resembling a mechanism referred as local fading,^[38] where the active material is disconnected from the surrounding matrix. If such particles reconnect in later stages, this may result in a temporary increase in electrode capacity.

2.3. Evolution of Electrode Strain and Local Dynamics

Using the in situ cycling at the ESRF, the temporal changes in microstructure were examined across three distinct swagelok cells: one during the first cycle (labelled as S1 representing "swagelok-cell cycle 1"), one during the 11th cycle (S11), and the other during the 21st, 22nd, and 23rd cycles (S21–23). The pre-cycled cells S11 and S21–23 exhibited typical electrochemical performance during tomography scans, consistent with the observations during pre-cycles at C/3 (refer supporting data Figure S5). However, for the cell right after formation during the first cycle, S1 did not cycle properly at C/3 it was thus decided to use C/8 to complete the full cycle. The performance of S1 was poor, and the capacity was lower than that anticipated for

the first cycle. It was also noted that during the initial formation step, the cell S1 had a CE of 55% with the final capacity of 411 mAh g^{-1} , which is very low compared to the usual capacity (refer supporting data Figure S4). In comparison to the coin cells, regulating the electrochemical performance of the swagelok cells is challenging since the electrodes are tiny, and the applied pressure is not reliable. Nevertheless, when observing the tomography results, the global evolution of the electrode seemed to correspond with the electrodes that exhibited good electrochemical performance (S11 and S21–23). Due to this, the global and local strain estimates for cell S1 are also presented here, keeping in mind its reduced electrochemical performance.

2.3.1. Global Strain Measure

Figures 5, 6A, and B illustrate the evolution of the electrodes during lithiation and delithiation of swagelok cells S1, S11 and S21–23 respectively. The potential and current variation plots are superimposed with global strain and SOL (refer to Equations (6) and (7)). The bottom X-axis represents the time in minutes and its replica on the top highlights the timestamps corresponding to the image acquisition time. The images corresponding to the key timestamps are presented near the plots for each sample; for a detailed overview of the dynamic evolution, refer to the supporting media. A preliminary scan, labelled as "Ref", was captured before the start of cycling, representing an initial reference state which was used as a reference for estimation of strain. The global strain represents the change in the overall displacement of the active material coating on the electrode. Given that the lateral displacement of

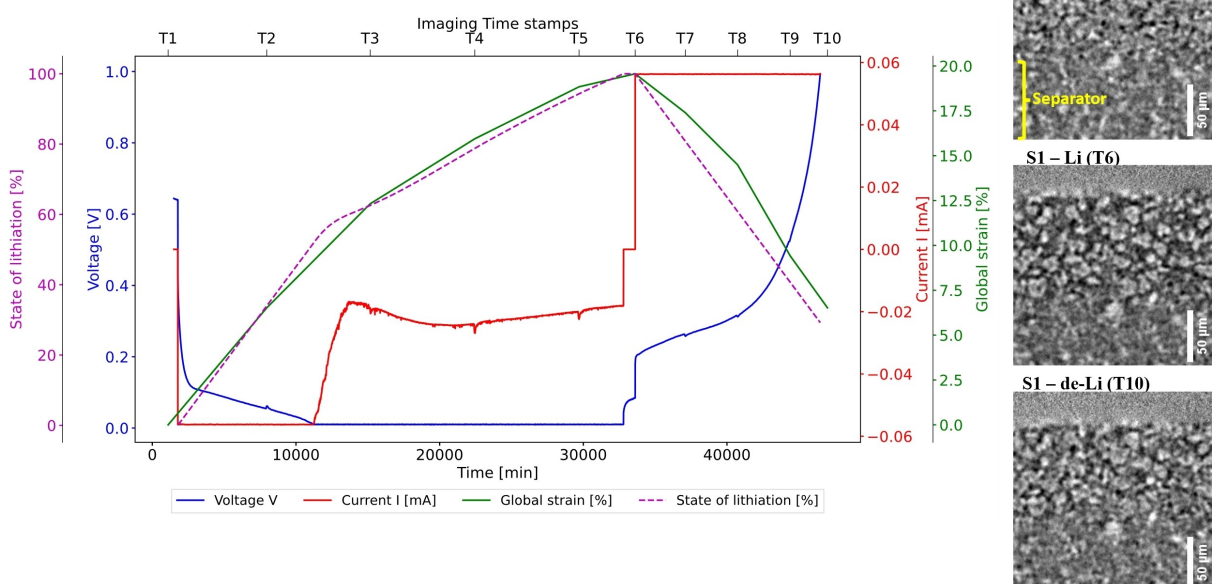


Figure 5. Left: Evolution of the electrode S1 during the first cycle presenting the global strain at each tomographic time stamp; Right: Key timestamps (T1, T6, and T10) corresponding to completely lithiated and delithiated states showing (current collector) (scale bar: 50 μm).

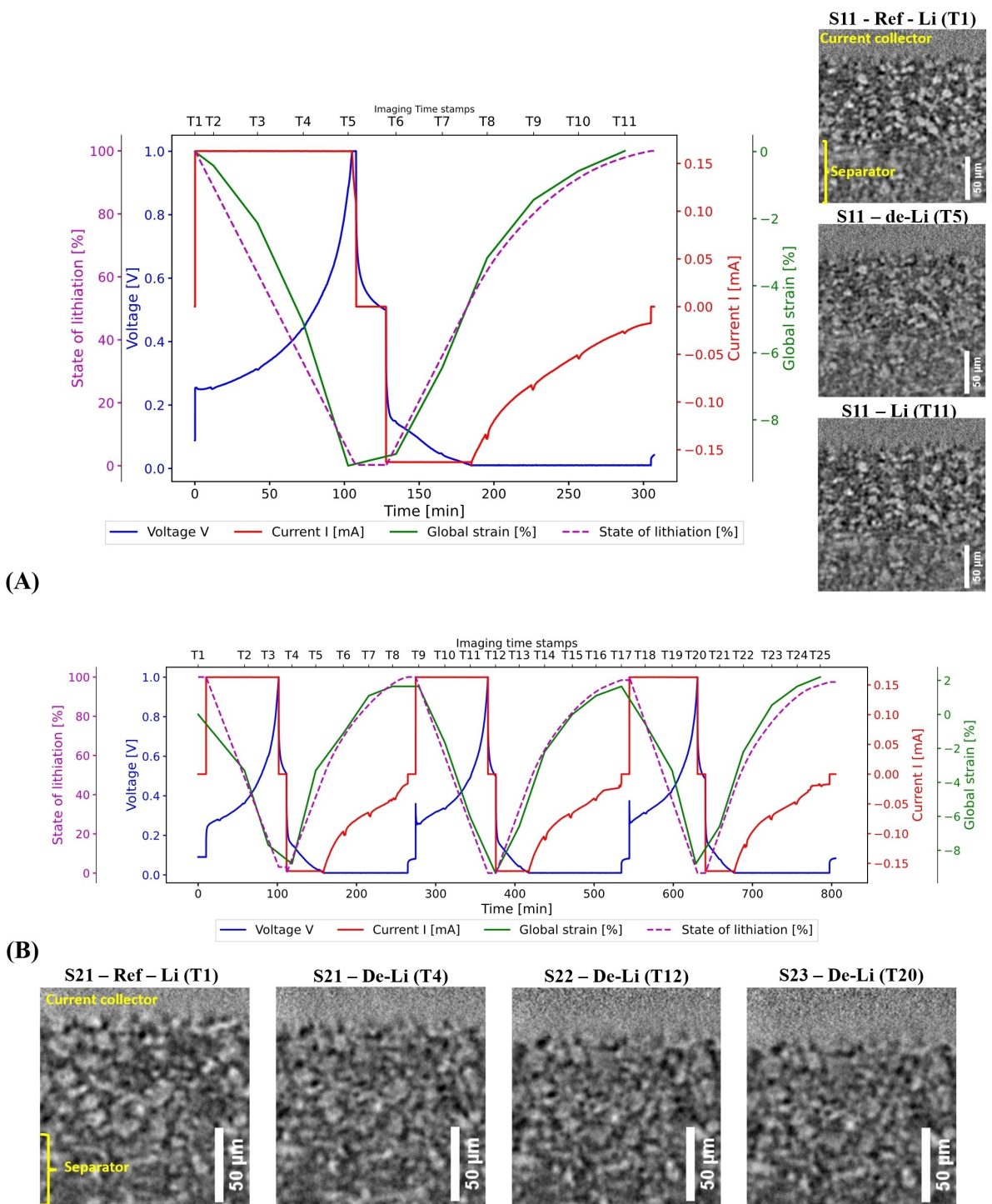


Figure 6. Evolution of current, voltage, and global strain of the electrodes (A) Cell S11: 11th cycle with corresponding images to its right side (scale bar: 50 μ m). (B) Cell S21–23: 21st, 22nd, and 23rd cycles with corresponding images below (scale bar: 50 μ m).

the electrode is minimal in comparison to the displacement along the coating thickness at the electrode scale, this study approximates global strain by focusing exclusively on the thickness variation of the active material coating. This was measured as shown in the Equation (6) below:

$$\varepsilon_{\text{global}} = (t_{\text{scan}} - t_{\text{ref}})/t_{\text{ref}} \quad (6)$$

Where, t_{scan} is the thickness of the electrode at a given acquisition time and t_{ref} is the thickness of the electrode observed in the reference initial image. Similarly, the SOL is estimated from the capacities observed during the cycling in reference to its maximum capacity (C_{\max}) as shown in Equation (7) below.

$$S = (C_{\max} - C)/C_{\max} \quad (7)$$

Three distinct regions can be identified for each sample: a copper current collector on top, a separator at the bottom, and the active material in between these regions are marked (in yellow) in the reference images of each electrode. At this pixel size (of $0.65\text{ }\mu\text{m}$), the differentiation between SiO_x and graphite particles is not clearly discernible. However, few particles can be partially identified at the central region of the electrode from completely lithiated states. For cell S1 (refer Figure 5), which shows the evolution of the electrode during its first cycle, the reference image corresponds to the completely delithiated state. During the lithiation stage, 4 images were taken at a regular interval of 120 min and among these, only one image was taken during the constant current lithiation (CC Li) step. Whereas, during the delithiation at constant current (CC DeLi) the image acquisition interval was reduced to 58 min. This can also be observed from the regular voltage and current variation recorded by the potentiostat during the scans due to the interaction of X-rays with the electrode. The maximum global strain in the electrode from reference to a completely lithiated state was observed to be 19.5%. The electrode did not completely return to its original thickness giving a residual strain of 6% during delithiation. The contribution of CC Li for the total strain was approximately 55% of the total strain during lithiation.

For precycled cells S11 and S21–23 (see Figure 6A and B) the reference state was completely lithiated. Once the reference images were taken, as these cells were cycled at C/3, in order to have a similar temporal resolution, scans were performed during the cycling at regular intervals of 30 min. For S11, A total of 11 tomography scans were performed (reference-1 image; CC DeLi-4 images; CC Li-2 images; CV Li-4 images). A global strain of approximately 9.4% was measured for the active material region at the completely delithiated state, which was almost completely recovered during followed re-lithiation. During relithiation the CC Li contributed to approximately 65% of the total strain.

Similarly, for cell S21–23, three successive cycles were imaged since the initial occurrence of scans during the 21st cycle was not optimally timed. An average of 9 scans were performed for each cycle. On the 21st cycle, a global max strain of -8.79% was measured at T4. The maximum strain measure was taken at T4. However, it was corresponding to the start of re-lithiation, as from cell S11 it can be noted that the difference in the strain did not seem to vary significantly between the end

of delithiation and the start of re-lithiation. Moreover, during the following re-lithiation, an electrode strain of approximately 2% is seen beyond the initial reference thickness. In the later cycles S22 and S23, an average global strain of -10% was measured for each cycle with an average contribution of 70% to the CC Li stage. The global strain in all the samples is summarized in Table 1, which shows a slightly decreasing trend with cycling.

2.3.2. Local Strain Measure

Global strain provides insights into the collective effect of silicon swelling at the electrode level as observed in the previous section. While local strain estimation reveals the deformation within specific electrode regions. From the tomographic observation, the breathing behavior of the electrode with lithiation/delithiation was observed (refer video on electrode evolution in supporting media), partially showing displacements in active material. Using these as the markers, the localized displacement and strain in the electrode can be measured at different locations within the electrode. By carrying out DVC on the previous samples, these additional details on the local strain evolution were extracted. Initially, for each sample, sub volumes of approximately $650\times650\times230\text{ pixel}^3$ ($422.5\times422.5\times149.5\text{ }\mu\text{m}^3$) were extracted from the overall in-situ tomo volume. These sub volumes were meshed using C8 elements with an element size of 8 pixels ($5.2\text{ }\mu\text{m}$ element size). A regularization size of 96 pixels ($62.4\text{ }\mu\text{m}$) was selected by trial and error and checking the convergence of DVC. The details regarding the effect of element size and regularization size are provided in the supporting data. The quality of the correlation was visually inspected (refer to the supporting data for the protocol).

Figure 7 presents the sub volume analyzed using DVC and their corresponding strain estimates at the maximum displacement state for each electrode (refer to supporting media for video on strain evolution of each sample). Islands of varying volumetric strains are observed in the active material region. When considering an element size of $5.2\text{ }\mu\text{m}$, these strains do not signify the volumetric strain of particles; rather, they denote localized effects imparted by the swelling particles. The volumetric strain in electrode S1 is positive since the reference state is de-lithiated. Whereas, for samples S11 and S21–23 this was negative. For the ease of comparison, the absolute values of volumetric strain were considered for electrodes S11 and S21–23 (see Figure 8). A decreasing trend is evident in the

Table 1. Summary of capacities and global strain in the electrodes (refer supporting data for evolution on lithiation/delithiation profiles).

| | S1 ^[a] 1st cycle | S11 11th cycle | S21 21st cycle | S22 22nd cycle | S23 23rd cycle |
|--------------------------------------|-----------------------------|----------------|----------------|----------------|----------------|
| Max capacity [mAh g ⁻¹] | 379 | 389 | 342 | 325 | 305 |
| Strain at complete de-lithiation [%] | – | -9.37 | -8.8 | -9.3 | -8.7 |
| Strain at relithiation [%] | 19.5 | 0 | 1.6 | 1.6 | 2.2 |

^[a] Cycled at C/8.

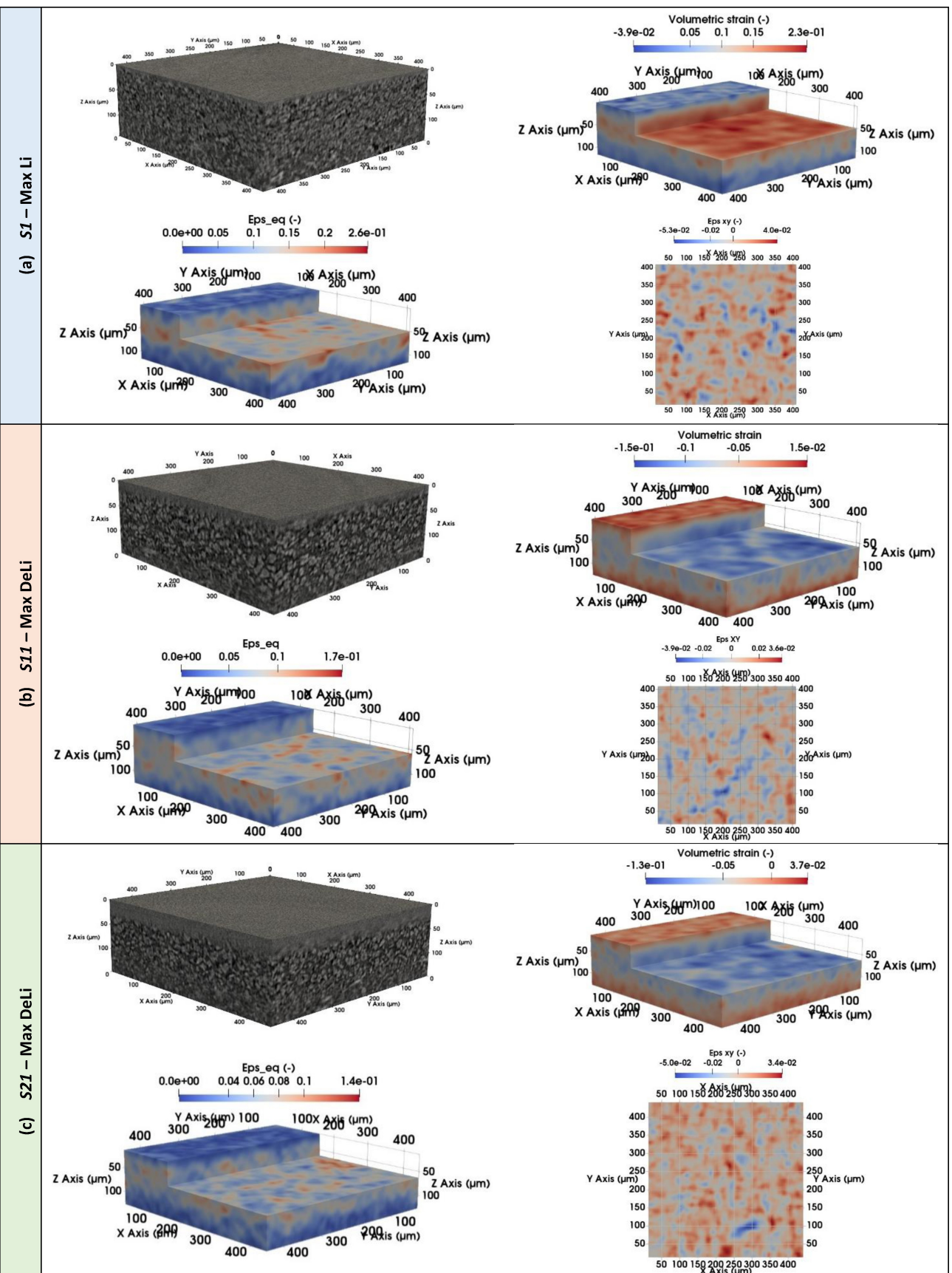


Figure 7. DVC results show the strain estimates in the active material region at the maximum displacement; (a)S11 (b)S11, and (c) S21. For each electrode; Top-Left: DVC Sub volumes, Top-Right: Volumetric strain (ϵ_v), Bottom-Left: Equivalent strain (ϵ_{eq}), Bottom-Right: Transversal shear component (ϵ_{xy}) in slice closer to the current collector.

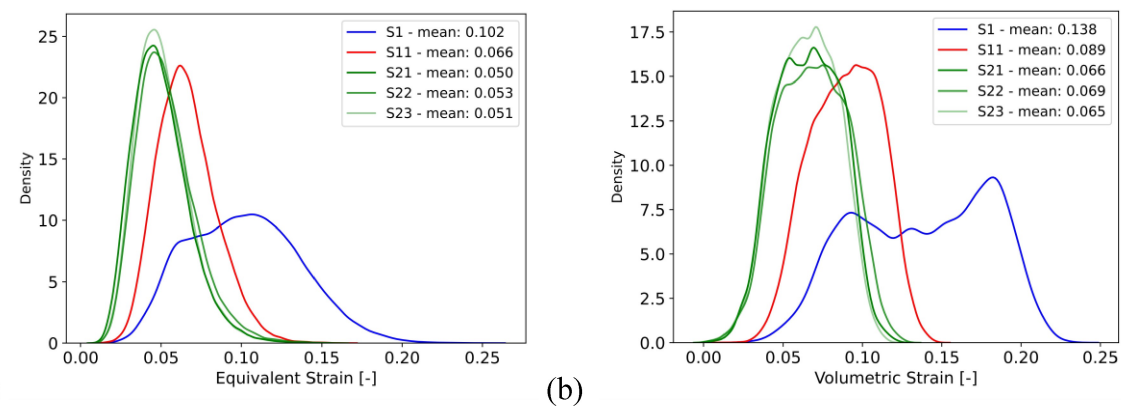


Figure 8. Histogram comparing the strain distribution measured in each cell. (a) Equivalent von Mises strain (ϵ_{eq}), (b) Volumetric strain (ϵ_v) (S1 superimposed with the absolute of S11 and S21–23).

volumetric strain with the increasing number of cycles. A large shift is seen from the first cycle to the 11th cycle, but this was not as significant from the 11th to the 21st cycle. The successive cycles 21, 22, and 23 did not show significant variation in the distribution. The strain distribution during the first cycle also showed a wide distribution with two peaks.

Regarding the von mises equivalent strain, a heterogeneous distribution is evident in the active material with localized regions of maximum strain. These local regions of strain can be potential starting points for crack initiation and propagation. Similar to the results of volumetric strain, cell S1 exhibits the maximum amount of strain variation (max: 25%, mean: 10%, and min: 1.6%), this is usually observed during the initial cycle and can have a significant impact on the binder. Considering the macroscopic mechanical properties of CMC from the literature,^[39] a local maximum strain of 6–10% or above might lead to failure of the binder. However, at microscale the properties of the materials are much different. But the microscale behavior of most of these binders is unknown, except for the recent investigation on PVDF by the authors of reference,^[40] which showed a significant variation in the properties. Moreover, the superior performance of CMC/SBR binder is often related to its self-healing properties and its adhesion strength over the surface of silicon. Compared with the other cells S11 and S21–23, the equivalent strain also seems to follow the same trend as the volumetric strain, gradually diminishing far below the failure strain of the binders (for example CMC/SBR). However, further cycling would likely damage the electrode due to fatigue. In addition to these, the region closer to the current collector shows a variation in the shear component (ϵ_{xy}) of strain. The shear strain near the current collector is crucial since it can fail the binder that is holding the active material attached to the current collector. Large shear strain in this region can lead to the delamination of the electrode from the current collector. The variation of ϵ_{xy} was observed to be similar in all three electrodes with the values centered around zero.

Overall, the analysis of the capacities and strains (both global and local) in the swagelok cells reveals varying trends across the cycling process. During the first cycle, compared to the 11th cycle, higher strain was observed (ϵ_{eq_mean} : 10.2%)

despite a slightly lower electrode capacity (S1: 379 mAh g⁻¹), suggesting that the factors influencing strain in the electrode extend beyond capacity alone. In contrast, during the 11th and 21–23rd cycles, the strain in the electrode appears to be more directly correlated to the electrode's capacity. This complex behavior might be influenced by several factors. One key factor is silicon swelling, which is directly related to the extent of lithiation of SiO_x particles and impacts capacity. Another potential factor is changes in the spatial arrangement and distribution of silicon particles within the electrode. During the initial cycles, these factors could result in higher strain despite lower capacity, but as cycling progresses and the system stabilizes, the relationship between strain and capacity may become more predictable. Further investigation on a single cell or modelling might be necessary to confirm this.

2.3.3. Residue from DVC

During the process of lithiation and de-lithiation, dark regions appeared both in the separator and the active material region. In the separator this was observed to be due to the evolution of gas such as H₂ and CO₂ which forms a low X-ray absorbing regions.^[29] Whereas, in the active material region this was identified to be due to the change of silicon-oxygen phase as observed from the post-mortem tomographs and the evolution of pore volume. The contrast changes in the active material region resulted in residue when solving the optical flow equation. However, this did not have a significant impact on the local strain estimations from DVC (refer to supporting data). To observe the evolution of residue, from cell S11 a location where there was gas evolution was selected and DVC estimate was performed. both the active material and separator zones for timestamps T5 and T11 are presented in Figure 9. As it can be noted by comparing the two states, the residue within the active region diminishes during subsequent lithiation, leaving very few remnants, demonstrating the reversibility of the contrast change in the active material region. This can be attributed to both the contrast changes due to the phase transformation and the changes in the gaps between the

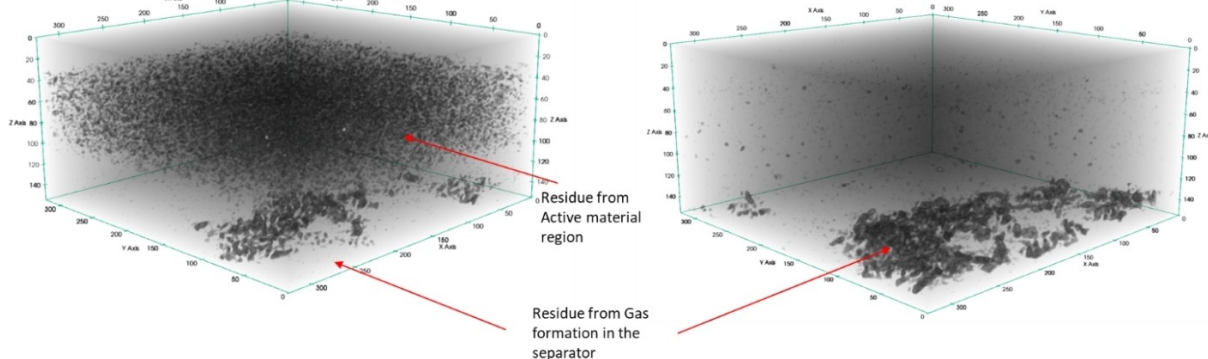


Figure 9. Appearance of residue in the active material and the separator regions for the 11th cycle Left: S11-De-Li(T5); Right: S11-Li(T11).

particles, which are filled by the liquid electrolyte. The residue in the active zone constitutes roughly 13% of the volume fraction of the active material region at T5. Additionally, the residue within the separator area displayed continuous evolution, indicating ongoing electrolyte decomposition leading to gas formation. This accounted for 3.5% of the segmented separator volume at T5 and 14% at T11. Similarly, for the sub volumes previously presented for the local strain analysis, only the active material region was analyzed as this was the region of interest for strain (Refer to the supporting data for the residue in these sub volumes).

2.3.4. Length Scales of the Strain

For characterizing the spatial variability of strain in the electrodes 3D implementation of the triangulation approach is used.^[41] Initially, strain values are normalized, and local extremes are identified by isolating the active material region and comparing each point within it to its 26 immediate neighboring points in 3D. Locations with strain values higher than all their neighbors were classified as local maxima, and a similar process was used to identify local minima. The identified local extrema were then used to perform a Delaunay tessellation (Figure 10a), the edges connecting the points located on the boundaries were removed to avoid the boundary effects. The lengths of all tessellation edges are measured, as depicted in Figure 10b through density plots. It was observed that the length scales of the volumetric strain and the equivalent strain are slightly different. This is because, In the case of volumetric strain, most maximum points are concentrated at the center, while minimum points occupy zones closer to the boundaries. In the case of the equivalent strain, the local extrema were more randomly distributed. In both scenarios, a trend is seen where the characteristic length to strain slightly decreases with an increasing number of cycles. The average length scales of equivalent strain varied from 42.3 μm for S1 to 33.7 μm for S23. In the case of volumetric strain, the mean length scale varied from 58.6 μm for S1 to 47.7 μm for S23. The variation in the characteristic length is in the range of the average diameter of the particles. Though the

strain values at the maximum displacement are very different between the electrodes the characteristic length did not change significantly. These length scales can serve as a parameter for comparing strain distribution in electrodes with similar formulations or when modelling electrode dynamics.

3. Conclusions

In this study, the microstructural features of the SiO_x/C negative electrode were characterized using a laboratory tomography at a pixel-size of 0.3 μm . From the cells after cycling, a heterogeneous mix of active, partially active, and inactive silicon oxide particles were observed. It was also seen that some of the silicon oxide particles exhibited local fading with temporary disconnection from the surrounding shell. Later, by employing In-situ tomography at the ESRF synchrotron, dynamic changes in the electrode structure, such as the global change in electrode thickness, contrast changes of silicon particles on lithiation, and gas evolution due to electrolyte decomposition, were observed. From the different swagelok cells tested, it was observed that the global strain decreases with cycling. By combining tomography with DVC, the evolution of local strain in the electrode was studied, and it was found that the local strain in the electrode was significant enough to cause damage to the binder especially in the first cycle. The relationship between capacity and strain in the electrode during initial cycles appeared complex, likely influenced by factors such as SiO_x particle spatial arrangement. As cycling continued, a more direct correlation between strain and capacity emerged. This should however be confirmed either through modelling or by observing strain evolution of a single electrode over initial 10 cycles. The spatial distribution of strain in the electrode was quantified using characteristic length. This characteristic length to strain can be used to compare the distribution of the strain field while modelling the electrode delamination. Additionally, the analysis of residue offered valuable insights into the impact of change of contrast within the electrode and the formation of gas due to electrolyte decomposition during lithiation and delithiation.

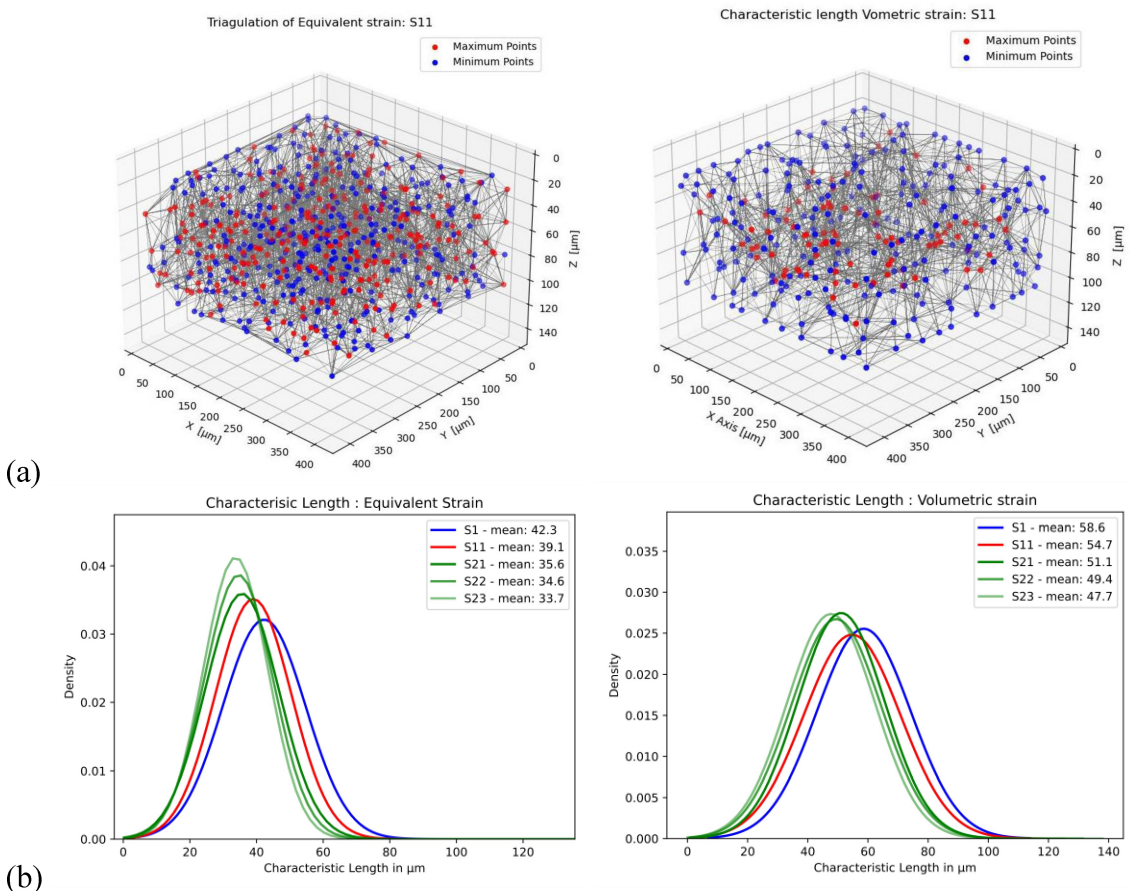


Figure 10. (A) Delaunay tessellation of extreme points; (B) distribution of the edge lengths of the tessellation. Left: Equivalent strain, right: Volumetric strain.

Acknowledgements

We would like to thank Samuel SIMAGA and Jordan LACORNE from INSA Lyon for their invaluable assistance in conducting in-situ experiments at the ESRF.

Conflict of Interests

The authors declare no conflict of interest.

Data Availability Statement

The data that support the findings of this study are available from the corresponding author upon reasonable request.

Keywords: Lithium-ion batteries • X-ray computed tomography • In situ imaging • Digital volume correlation • Mechanical degradation • Local strain

[1] Nationale Plattform zukunft der mobilität, *Roadmap Integrated Cell and Battery Production Germany*, 2016. <https://www.plattform-zukunft-mobilitaet.de/2download/roadmap-integrierte-zell-und-batterieproduktion-deutschland>.

- [2] K. R. Kganyago, P. E. Ngoepe, *Phys. Rev. B* **2003**, *68*, 205111.
- [3] J. Asenbauer, T. Eisenmann, M. Kuenzel, A. Kazzazi, Z. Chen, D. Bresser, *Sustainable Energy Fuels* **2020**, *4*, 5387.
- [4] Y. Jin, B. Zhu, Z. Lu, N. Liu, J. Zhu, *Adv. Energy Mater.* **2017**, *7*, 1700715.
- [5] H. Kim, C.-Y. Chou, J. G. Ekerdt, G. S. Hwang, *J. Phys. Chem. C* **2011**, *115*, 2514.
- [6] J. W. Choi, D. Aurbach, *Nat. Rev. Mater.* **2016**, *1*, 1.
- [7] C. R. Birk, M. R. Roberts, E. McTurk, P. G. Bruce, D. A. Howey, *J. Power Sources* **2017**, *341*, 373.
- [8] M. Ashuri, Q. He, L. L. Shaw, *Nanoscale* **2016**, *8*, 74.
- [9] M. A. Al-Maghribi, J. Suzuki, R. J. Sanderson, V. L. Chevrier, R. A. Dunlap, J. R. Dahn, *J. Electrochem. Soc.* **2013**, *160*, A1587–A1593.
- [10] S. C. Jung, H.-J. Kim, J.-H. Kim, Y.-K. Han, *J. Phys. Chem. C* **2016**, *120*, 886.
- [11] F. Silveri, M. Alberghini, V. Esnault, A. Bertinetto, V. Rouchon, M. Giuliano, G. Gudendorff, C. Zhao, J. Bikard, M. Sgroi, A. Tommasi, M. Petit, *J. Power Sources* **2024**, *598*, 234109.
- [12] S. Schweißler, L. de Biasi, A. Schiele, P. Hartmann, T. Brezesinski, J. Janek, *J. Phys. Chem. C* **2018**, *122*, 8829.
- [13] P. Heugel, J. Petit, F. Klein, J. Tübke, *Batteries* **2023**, *9*, 449.
- [14] V. Vanpeene, A. King, E. Maire, L. Roué, *Nano Energy* **2019**, *56*, 799.
- [15] J. Gonzalez, K. Sun, M. Huang, J. Lambros, S. Dillon, I. Chasiotis, *J. Power Sources* **2014**, *269*, 334.
- [16] O. O. Taiwo, J. M. Paz-García, S. A. Hall, T. M. Heenan, D. P. Finegan, R. Mokso, P. Villanueva-Pérez, A. Patera, D. J. Brett, P. R. Shearing, *J. Power Sources* **2017**, *342*, 904.
- [17] D. P. Finegan, A. Vamvakarios, L. Cao, C. Tan, T. M. M. Heenan, S. R. Daemi, S. D. M. Jacques, A. M. Beale, M. Di Michiel, K. Smith, D. J. L. Brett, P. R. Shearing, C. Ban, *Nano Lett.* **2019**, *19*, 3811.
- [18] B. Pan, K. Qian, H. Xie, A. Asundi, *Meas. Sci. Technol.* **2009**, *20*, 62001.
- [19] A. Ulvestad, J. N. Clark, A. Singer, D. Vine, H. M. Cho, R. Harder, Y. S. Meng, O. G. Shpyrko, *Physical Chemistry Chemical Physics PCCP* **2015**, *17*, 10551.
- [20] A. Ulvestad, A. Singer, H.-M. Cho, J. N. Clark, R. Harder, J. Maser, Y. S. Meng, O. G. Shpyrko, *Nano Lett.* **2014**, *14*, 5123.

- [21] Y. Qi, S. J. Harris, *J. Electrochem. Soc.* **2010**, *157*, A741.
- [22] P. K. Leung, C. Moreno, I. Masters, S. Hazra, B. Conde, M. R. Mohamed, R. J. Dashwood, R. Bhagat, *J. Power Sources* **2014**, *271*, 82.
- [23] D. P. Finegan, E. Tudisco, M. Scheel, J. B. Robinson, O. O. Taiwo, D. S. Eastwood, P. D. Lee, M. Di Michiel, B. Bay, S. A. Hall, G. Hinds, D. J. L. Brett, P. R. Shearing, *Advanced Science (Weinheim, Baden-Wurttemberg, Germany)* **2016**, *3*, 1500332.
- [24] J. M. Paz-Garcia, O. O. Taiwo, E. Tudisco, D. P. Finegan, P. R. Shearing, D. Brett, S. A. Hall, *J. Power Sources* **2016**, *320*, 196.
- [25] D. S. Eastwood, V. Yufit, J. Gelb, A. Gu, R. S. Bradley, S. J. Harris, D. J. L. Brett, N. P. Brandon, P. D. Lee, P. J. Withers, P. R. Shearing, *Adv. Energy Mater.* **2014**, *4*, 1300506.
- [26] P. Pietsch, D. Westhoff, J. Feinauer, J. Eller, F. Marone, M. Stampanoni, V. Schmidt, V. Wood, *Nat. Commun.* **2016**, *7*, 12909.
- [27] MSE Supplies, *SiO_x/Cy Composite Silicon based Anode: SKU no. PO0197, 2020.* <https://www.msesupplies.com/products/mse-pro-siox-c-composite-silicon-based-anode-powder-for-lithium-ion-battery-500g?variant=31835988164666>.
- [28] Z. Karkar, T. Jaouhari, A. Tranchot, D. Mazouzi, D. Guyomard, B. Lestriez, L. Roué, *J. Power Sources* **2017**, *371*, 136.
- [29] V. Vanpeene, A. Etiemble, A. Bonnin, E. Maire, L. Roué, *J. Power Sources* **2017**, *350*, 18.
- [30] S. Bazlen, P. Heugel, O. von Kessel, W. Commerell, J. Tübke, *J. Storage Mater.* **2022**, *49*, 104044.
- [31] C. K. Christensen, M. A. Karlsen, A. Ø. Drejer, B. P. Andersen, C. L. Jakobsen, M. Johansen, D. R. Sørensen, I. Kantor, M. R. V. Jørgensen, D. B. Ravnsbæk, *J. Synchrotron Radiat.* **2023**, *30*, 561.
- [32] J. Lachambre, *Développement d'une méthode de caractérisation 3D des fissures de fatigue à l'aide de la corrélation d'images numériques obtenues par tomographie X* **2014**.
- [33] J. Lachambre, *pyFEDIC*, Zenodo **2023**.
- [34] G. Besnard, H. Leclerc, F. Hild, S. Roux, N. Swiergiel, *J. Strain Anal. Eng. Des.* **2012**, *47*, 214.
- [35] D. Ayala, I. Cruz-Matías, S. Gutsch, D. Hiller, S. Estradé, M. Zacharias, F. Peiró, *J. Comput. Sci.* **2019**, *30*, 28.
- [36] V. Vanpeene, J. Villanova, J.-P. Suuronen, A. King, A. Bonnin, J. Adrien, E. Maire, L. Roué, *Nano Energy* **2020**, *74*, 104848.
- [37] R. Yu, Y. Pan, Y. Jiang, L. Zhou, D. Zhao, G. van Tendeloo, J. Wu, L. Mai, *Adv. Mater. (Deerfield Beach, Fla.)* **2023**, *35*, e2306504.
- [38] I. Choi, M. J. Lee, S. M. Oh, J. J. Kim, *Electrochim. Acta* **2012**, *85*, 369.
- [39] J. Li, R. B. Lewis, J. R. Dahn, *Electrochim. Solid-State Lett.* **2007**, *10*, A17.
- [40] A. H. Iyer, P. Gupta, P. Gudmundson, A. Kulachenko, *Mater. Sci. Eng. A* **2023**, *881*, 145352.
- [41] M. Alves, Y. Li, S. Pimenta, *Compos. Part B* **2023**, *262*, 110789.

Manuscript received: June 27, 2024

Revised manuscript received: August 28, 2024

Accepted manuscript online: September 20, 2024

Version of record online: November 4, 2024